

Mathematical textbook of deformable neuroanatomies

MICHAEL I. MILLER*, GARY E. CHRISTENSEN*, YALI AMIT†, AND ULF GRENANDER‡

*Department of Electrical Engineering and the Institute for Biomedical Computing, Washington University, St. Louis, MO 63130; †Department of Statistics, University of Chicago, Chicago, IL 60637; and ‡Division of Applied Mathematics, Brown University, Providence, RI 02912

Communicated by Lawrence Shepp, April 23, 1993

ABSTRACT Mathematical techniques are presented for the transformation of digital anatomical textbooks from the ideal to the individual, allowing for the representation of the variabilities manifest in normal human anatomies. The ideal textbook is constructed on a fixed coordinate system to contain all of the information currently available about the physical properties of neuroanatomies. This information is obtained via sensor probes such as magnetic resonance, as well as computed axial and emission tomography, along with symbolic information such as white- and gray-matter tracts, nuclei, etc. Human variability associated with individuals is accommodated by defining probabilistic transformations on the textbook coordinate system, the transformations forming mathematical translation groups of high dimension. The ideal is applied to the individual patient by finding the transformation which is consistent with physical properties of deformable elastic solids and which brings the coordinate system of the textbook to that of the patient. Registration, segmentation, and fusion all result automatically because the textbook carries symbolic values as well as multisensor features.

Global Shape Models and Anatomical Templates

Imaging modalities such as magnetic resonance (MR) imaging, x-ray computed tomography (CT), and positron emission tomography (PET) provide exquisitely detailed *in vivo* information regarding the anatomy and physiological function of specific subjects. However, the interpretation of the data has been hindered by the inability to expeditiously relate such information to specific anatomical regions. The difficulty lies in two areas: images from atlases and other modalities must be registered; but more fundamentally, even when registered, normal variation in anatomy makes interpretation extremely difficult. This paper provides algorithms for representing normal neuroanatomies by precisely specifying the global anatomical relationships between structures and how they can vary from one individual to another. The goal is to provide representations which allow for the generalization of a single electronic anatomical textbook to the individual.

Accommodating the variability manifest in human anatomies is an ambitious goal. There is no shortage of image processing algorithms designed to improve pictures by noise suppression or to recognize particular patterns so as to segment pictures into subpictures. Much of the greatest success has been with algorithms that model sensor variability, such as for x-ray, MR, or emission tomography.

But the variability in the anatomical shapes and structures themselves is much less well understood. The main difficulty is that human anatomies form highly complex systems. Browsing through an anatomical textbook, one is struck by the awesome amount of information. The enormous complexity of biological patterns makes the design of representations of even normal anatomies a difficult, not to say

overwhelming, endeavor. Limitations of existing methods become visible for such ambitious tasks as representation of the shape ensemble itself. Since the mid 1970s researchers have built models that attempt to incorporate structured variability. The early paper of Besag (1) began the line of research on the use of probabilistic Markov random-fields (MRF) models for texture analysis. The MRF approach has demonstrated a good deal of success in image restoration and segmentation. But this is not enough for representing the global relations illustrated by the typical aforementioned anatomies. Natural textures can be modeled with MRFs, since most of their variability is of a local nature: the probabilistic dependencies extend over a quite limited range.

To meet the greater challenge of representing the anatomical relations between structures in human anatomies, global representations must be employed. Mathematical techniques for such representations began to appear in the early 1980s under the name of "global shape" models. The global shape models represent image ensembles in terms of their typical structure via the construction of templates, and their variabilities by the definition of probabilistic transformations that are applied to the templates. The transformations form groups (translation, scale, and rotation) and are applied to the template, in this case an electronic atlas, so that a rich family of shapes may be generated with the global properties of the templates maintained.

There has already been a vast body of work on multimodality image fusion and registration (see ref. 2 for a substantive introduction). The simplest methods of registration used assume that the images or tissues being matched are highly similar ones for which only global, course features must be matched. Transformations of this type consist of rigid global rotation and translation and/or simple scaling. We, however, are interested in accounting for very local variability across disparate anatomies, thereby requiring high-dimensional transformations on the coordinate system, of dimension proportional to the size of the voxel lattice. Alternatively, many investigators have taken the approach of defining a small set of features—fiducial markers and/or landmarks—which drive the registration. In the method proposed here, the multisensor tomographic data directly provide the driving force for the transformation and alignment of the coordinate systems. If fiducial markers and landmarks are also defined, they become powerful boundary conditions for our method, but they are not required.

The work proposed herein is most akin to the physically based modeling work of Terzopoulos (see ref. 3, for example) in which transformations are constructed to obey certain physical laws. Most relevant is the elegant work of Bajcsy and collaborators (4), which began in the early 1980s and in which deformable volume models were developed. The approach presented here, while identical in spirit to both, substantially differs and extends the previous methods. First, the driving force acting throughout the continuum is the

nonlinear variation of the distortion between the deforming template and the multimodality imaging data. The full nonlinear optimization is solved without linearization of the driving force. Only under the condition that the template and data are sufficiently similar so that the deformations are small do the linearized solutions give equivalent results (see ref. 5). Second, the deformation procedure is accomplished by solving a sequence of optimization problems from course to fine scale via parametrically defined deformation fields. This is analogous to multigrid methods, but here the notion of refinement from course to fine is accomplished by increasing the number of basis components in the series extension of the vector field. The final stage is to use the translation vector field over the entire continuum.

Our previous work on deformable templates for biological shape representation (6–9) involved templates of low complexity which could be constructed with modest effort. For example, organelles in electron micrographs such as membranes and mitochondria are generated as transformations of linear and elliptic shapes. Likewise, amoeba are modeled as transformations of a sphere. Constructing templates for human anatomies is a task orders of magnitude larger. The proposed neurological templates consist of megabytes of constants associated with three-dimensional images from sensor probes and symbolic textbook labeling. Until recently the construction of the template itself seemed to be the major obstacle for the successful application of these methods. It was therefore a welcome surprise to learn of the The Visible Human (10) project undertaken by the National Library of Medicine (NLM) in which digital anatomical templates are being constructed for two complete human beings. We quote from the NLM: “This Visible Human project would include digital images derived from computerized tomography, magnetic resonance imagery, and photographic images from cryosectioning of cadavers.” Initiatives such as this one make the proposed work particularly timely.

Anatomical Textbook and Transformations

The anatomical textbook (template) is a vector function defined on the ideal coordinate system of the textbook. The range of the template is real as well as symbolic in value, with the vector of values including measures of the intrinsic composition of the tissue associated with the various noninvasive sensor modalities, as well as anatomical label and histological information. The multivalued vector contains values associated with various imaging probes, MR spin-density, t1, and t2 images; CT attenuation density images; and functional PET images. Symbolic information would include the various labeled areas: white-matter tracts, gray-matter nuclei, Broca’s areas, etc.

The textbook is a vector mapping of the coordinate system $\Omega \subset \mathbb{R}^3$ according to $T: \Omega \rightarrow \mathcal{T}$, with the range space, \mathcal{T} , assumed to be an M -fold product of spaces $\mathcal{T}_1 \times \mathcal{T}_2 \times \dots \times \mathcal{T}_M$, where each component $T_m \in \mathcal{T}_m$ corresponds to a different feature of the tissue. The triple (Ω, T, \mathcal{T}) is termed the *anatomical textbook (template)*.

There are two kinds of variations which must be accommodated: normal variation among humans and variation due to diseased or abnormal states. Disease and abnormal variation is not addressed in this paper. Focusing on normal human variation, a set of transformations $h \in \mathcal{H}$ on the ideal coordinate system is defined where \mathcal{H} is the set of homeomorphic maps $h: \Omega \rightarrow \Omega$. The homeomorphisms are generated from translation groups applied to points $\mathbf{x} \in \Omega$:

$$h: \mathbf{x} = (x_1, x_2, x_3) \rightarrow [x_1 - u_1(\mathbf{x}), x_2 - u_2(\mathbf{x}), x_3 - u_3(\mathbf{x})]. \quad [1]$$

The vector field $\mathbf{u}(\mathbf{x}) = [u_1(\mathbf{x}), u_2(\mathbf{x}), u_3(\mathbf{x})]$ is called the displacement field. The maps constructed from these trans-

formations allow for the dilation and contraction of the underlying coordinates of the template into the coordinates of the individual anatomy at a very local level. The set of normal anatomies generated from the textbook (Ω, T, \mathcal{T}) becomes $\{T \circ h: h \in \mathcal{H}\}$, with \circ the composition operator.

Applying the Textbook. The anatomical textbook is applied to individual patients as follows. A *patient* is characterized via a *study* S , an N -valued vector function consisting of N -characterizing data sets $\{S_n\}_{n=1}^N$, or *substudies*. Each sub-study is an examination of the patient’s brain tissue via some sensor. It is assumed that all of the study types already exist in the *ideal* textbook which implies $S_n: \Omega \rightarrow \mathcal{T}_{m_n}$, for some $m_n \in \{1, 2, \dots, M\}$. For the work described here, the study modalities are assumed to be acquired in register; in general, a second processing step would be required to register modalities from a single patient. The information in the anatomical textbook (Ω, T, \mathcal{T}) is brought into the coordinates of the patient by finding the transformation $h \in \mathcal{H}$ on Ω which registers the studies $\{S_n\}_{n=1}^N$ with the textbook.

Registration between the template and study is defined by using a distance measure between the transformed textbook and the study with the distance equaling zero if and only if the two are equal. For all of the MR data, the squared-error distance $1/2\sigma^2 \int_{\Omega} \sum_{n=1}^N |T_n(\mathbf{x} - \mathbf{u}(\mathbf{x})) - S_n(\mathbf{x})|^2 d\mathbf{x}$ is used, which is consistent with Gaussian noise models in MR.

Mechanoelastic Energy Density. To ensure that the vector field of Eq. 1 results in transformations which are physically smooth, so that structures are not broken apart, it is assumed that they arise from a prior distribution with potential determined by the kinematics of elastic solids (11). This “Bayesian view” of the estimation problem gives rise to an associated potential of the posterior distribution, the sum of the distance and elasticity potentials,

$$H(\mathbf{u}) = \frac{1}{2\sigma^2} \int_{\Omega} \sum_{n=1}^N |T_n(\mathbf{x} - \mathbf{u}(\mathbf{x})) - S_n(\mathbf{x})|^2 d\mathbf{x} + \frac{\alpha}{2} \sum_{i=1}^3 \sum_{j=1}^3 \int_{\Omega} \left[\lambda \left(\frac{\partial u_i(\mathbf{x})}{\partial x_i} \right) \left(\frac{\partial u_j(\mathbf{x})}{\partial x_j} \right) + \mu \left(\frac{\partial u_i(\mathbf{x})}{\partial x_j} + \frac{\partial u_j(\mathbf{x})}{\partial x_i} \right)^2 \right] d\mathbf{x}, \quad [2]$$

where λ and μ are the Lamé elasticity constants and α is a Lagrange multiplier. In two or three dimensions both the likelihood term and the elasticity potential do not generate proper distributions on any function space. In practice, however, these transformations are approximated on the pixel lattice, the integrals becoming sums and the derivatives becoming differences (see below). In that context Eq. 2 yields a perfectly valid potential.

Algorithm: Stochastic Gradient Search

The method of solution is to generate the transformation field \mathbf{u} , which is the mean of the posterior distribution induced by the potential of Eq. 2. For this stochastic gradient, algorithms are proposed which follow gradients of the potential $H(\mathbf{u})$ with an additive noise term. Under proper conditions (7, 12) averages of the parameter estimates generated from the gradient algorithm converge to the mean which becomes the estimated transformation field shown in all of the results below. We note that because of finite averaging we are only assured that the mean of the posterior distribution is computed locally around the large energy minima. For all of the results, the three-dimensional prior is reduced to the two-dimensional prior in the following standard way. Assume that the stresses in the x_3 direction and the shear stresses in the $x_{1,3}$ and $x_{2,3}$ directions are zero, which

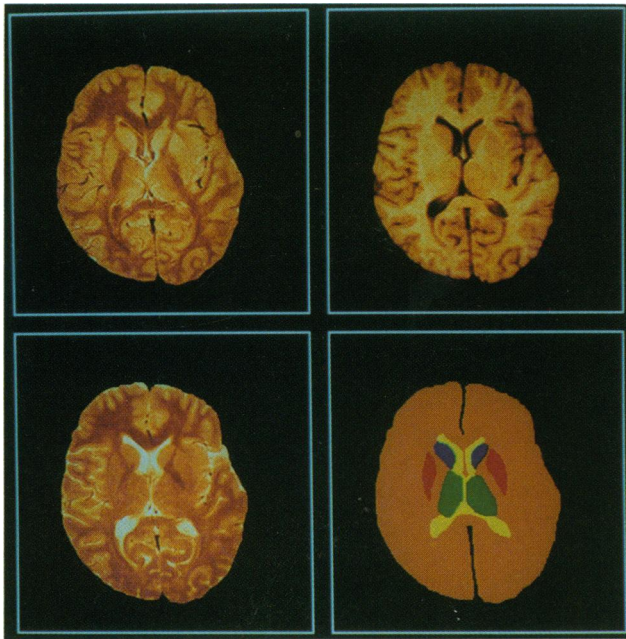


FIG. 1. Textbook components: spin-density (Upper Left), t1-weighted (Upper Right), and t2-weighted (Lower Left) MR images and a hand segmentation (Lower Right).

implies that $\partial u_3/\partial x_1 = -\partial u_1/\partial x_3$, $\partial u_3/\partial x_2 = -\partial u_2/\partial x_3$, and $\partial u_3/\partial x_3 = -[\lambda/(\lambda + 2\mu)][(\partial u_1/\partial x_1) + (\partial u_2/\partial x_2)]$. In two dimensions the constants $\eta_1 = (3\lambda\mu + 2\mu^2)/(\lambda + \mu)$ and $\eta_2 = \lambda/(2\lambda + 2\mu)$ will be extremely helpful. The estimation is accomplished in two steps: first through a low-dimensional parametric basis (7), and second through a high-dimensional parameterization which corresponds to estimating the translation field over the pixel lattice.

Low-Dimensional Coarse Refinement. The basis representation of the transformation field becomes

$$\mathbf{u}(\mathbf{x}) = \sum_{i,j=0}^d \frac{2^{1/2}}{(i^2 + j^2)^{1/2}} [\mu_{i,j,1} \mathbf{e}_{i,j,1}(\mathbf{x}) + \mu_{i,j,2} \mathbf{e}_{i,j,2}(\mathbf{x})] \quad [3]$$

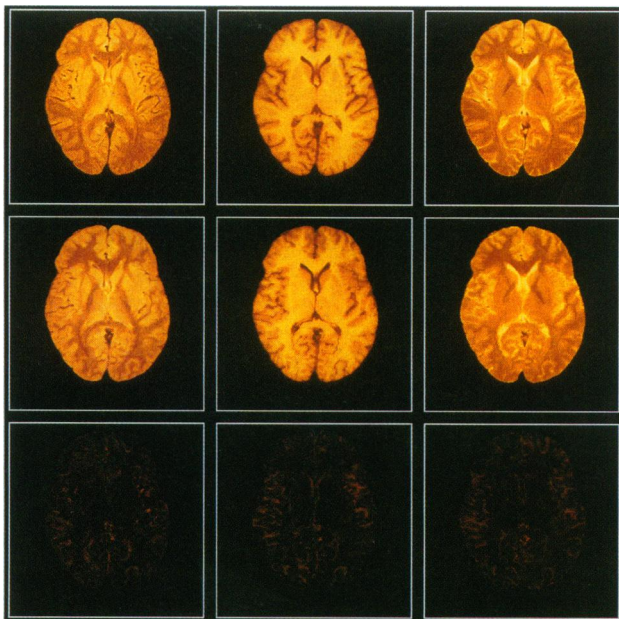


FIG. 2. (Top) Spin-density (Left), t1-weighted (Center), and t2-weighted (Right) images of patient A. (Middle) The transformed textbook. (Bottom) Magnitude difference images between the transformed textbook and the patient.

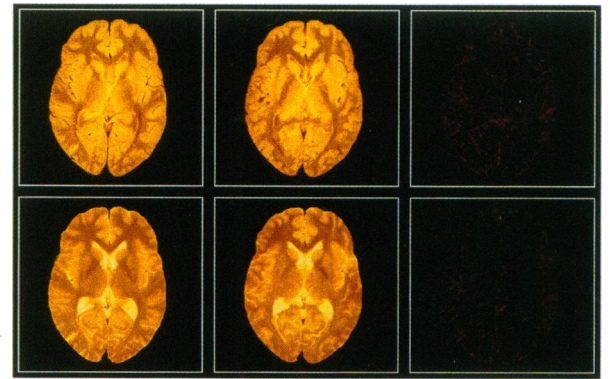


FIG. 3. (Left) Spin-density (Upper) and t2 (Lower) images of patient B. (Center) The transformed textbook. (Right) Magnitude difference images between the textbook and the patient.

with the pair of basis functions

$$\begin{aligned} \mathbf{e}_{i,j,1}(\mathbf{x}) &= \begin{pmatrix} i \sin \pi x_1 \cos \pi j x_2 \\ j \cos \pi x_1 \sin \pi j x_2 \end{pmatrix}, \\ \mathbf{e}_{i,j,2}(\mathbf{x}) &= \begin{pmatrix} -j \sin \pi x_1 \cos \pi j x_2 \\ i \cos \pi x_1 \sin \pi j x_2 \end{pmatrix}, \end{aligned} \quad [4]$$

chosen to diagonalize the covariances associated with the elasticity operator. The stochastic algorithm generates the expansion coefficient set $\{\mu_{i,j,1}, \mu_{i,j,2}\}_{i,j=0}^d$ according to

$$d\mu_{i,j,p}(t) = -\frac{1}{2} \frac{\partial H(\mathbf{u}(t))}{\partial \mu_{i,j,p}} dt + dw_{i,j,p}(t) \quad [5]$$

for $p = 1, 2$, where $w_{i,j,p}(t)$ is a Wiener process. The gradient of the potential with respect to the coefficients becomes

$$\begin{aligned} \frac{\partial}{\partial \mu_{i,j,p}} H(\mathbf{u}) &= -\frac{1}{\sigma^2} \int_{\Omega} \sum_{n=1}^N (T_n(\mathbf{x} - \mathbf{u}(\mathbf{x}, t)) - S_n(\mathbf{x})) \\ &\quad \times \nabla T_n(\mathbf{x} - \mathbf{u}(\mathbf{x}, t)) \cdot \mathbf{e}_{i,j,p}(\mathbf{x}) d\mathbf{x} + \alpha \beta_p (i^2 + j^2) \mu_{i,j,p}(t), \end{aligned} \quad [6]$$

with $\mathbf{a} \cdot \mathbf{b}$ denoting dot product, $\nabla T = [\partial T/\partial x_1, \partial T/\partial x_2]$, $\beta_1 = \eta_1 \pi^2/2(1 - \eta_2^2)$, and $\beta_2 = \eta_1 \pi^2/4(1 + \eta_2)$.

High-Dimensional Fine Search. The full optimization is solved at the highest resolution supported by the textbook; in this case the MR data is on a 256×256 pixel lattice \mathcal{L} . The continuous displacement field \mathbf{u} is approximated by the set $\{\mathbf{u}(\mathbf{l})\}_{\mathbf{l} \in \mathcal{L}}$ at each of the 256^2 lattice sites. The transformation field is estimated by stochastic gradient search according to

$$du_p(\mathbf{l}, t) = -\frac{1}{2} \frac{\partial H(\mathbf{u}(t))}{\partial u_p(\mathbf{l})} dt + dw_{\mathbf{l},p}(t), \quad [7]$$

where the parametric solution from Eq. 5 is used as the starting point. The partial derivatives $\partial H(\mathbf{u}(t))/\partial u_p(\mathbf{l})$ are obtained from the variational calculus gradient

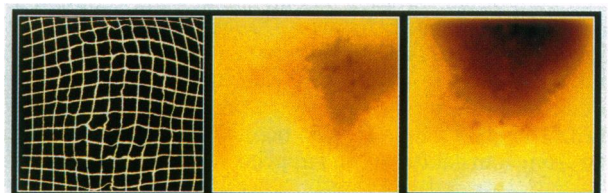


FIG. 4. (Left) Transformation between the textbook and patient B applied to the rectangular grid. (Center and Right) The x and y components of the transformation.

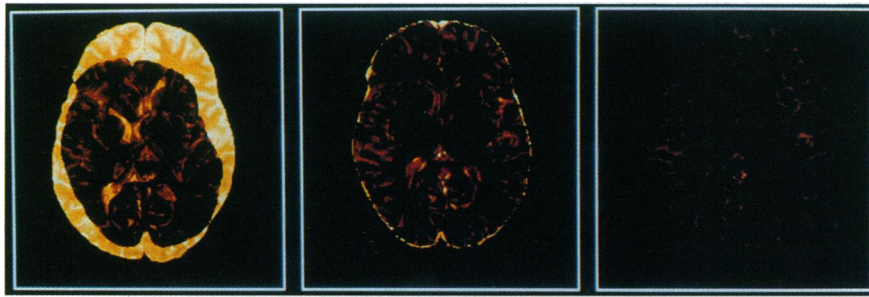


FIG. 5. Magnitude difference images between the t2 component of patient A and the textbook (Left), the globally deformed textbook (Center), and the locally deformed textbook (Right).

$$\delta H(\mathbf{u}) = \frac{\eta_1}{2(1 + \eta_2)} \nabla^2 \mathbf{u}(\mathbf{x}, t) + \frac{\eta_1}{2(1 - \eta_2)} \nabla \left(\sum_{p=1}^2 \frac{\partial u_p(\mathbf{x}, t)}{\partial x_p} \right) - \frac{1}{\sigma^2} \sum_{n=1}^N (T_n(\mathbf{x} - \mathbf{u}(\mathbf{x}, t)) - S_n(\mathbf{x})) \nabla T_n(\mathbf{x} - \mathbf{u}(\mathbf{x}, t)).$$

[8]

Here ∇^2 is the Laplacian operator. The lattice partial derivatives $\partial H(\mathbf{u}(t))/\partial u_p(\mathbf{l})$ ($p = 1, 2$) are obtained via discretization of the partial differential Eq. 8 by using standard symmetric difference lattice approximations.

For all of the results shown, d was systematically increased from 1 to 5 with 40 iterations of the stochastic gradient search run for each dimension. The standard deviation σ and simulation time step were 0.01 and 5×10^{-8} , respectively. The parametrically defined transformation field was then used as initial conditions to the high 2×256^2 dimensional search. Eq. 7 was run to equilibrium over 200 iterations, and then 50 iterations were used to generate the empirically averaged \mathbf{u} field. The standard deviation was kept the same, with the step size increased to 10^{-5} and the constants $\alpha\eta_1 = 0.01$ and $\eta_2 = 0.0$. Observe that omitting the noise term in Eqs. 5 and 7 transforms them into gradient descent equations leading to local minima corresponding to local maximum *a posteriori* solutions.

Results

Constructing and Generalizing the Textbook. A two-dimensional textbook was constructed from an MR study of a normal patient at Duke University using standard MR spin-echo sequences to generate a spin-density, t1-weighted, and t2-weighted series. A hand segmentation was also performed of the two-dimensional scans into the various gray-matter nuclear regions: thalamus, putamen, head of caudate nucleus, ventricle, other brain matter, and background. The textbook consists of a 4-tuple of three MR images and a hand-labeled segmentation. These are shown in Fig. 1. The hand-segmented labeling of the textbook (Fig. 1 Lower Right) was generated by using all three MR images, along with the detailed horizontal brain section on page 28 of the DeArmond *et al.* (13) anatomy atlas.

Two different patient studies, A and B, were analyzed. Study A consisted of $N = 3$ substudies (spin-density, t1-weighted, and t2-weighted MR images), and study B consisted of $N = 2$ substudies (spin-density and t2-weighted MR images). The studies were selected because of their similar orientations and level in the brain and not for their closeness in brain size or similarity to the textbook.

The result of estimating the transformation \hat{h}_A from the first experiment is shown in Fig. 2. The top row shows the spin-density (Left), t1-weighted (Center), and t2-weighted images (Right) from patient A. Shown in the middle row is the MR textbook of Fig. 1, transformed to patient A: the spin-density $T_1 \circ \hat{h}_A$ (Left), the t1 image $T_2 \circ \hat{h}_A$ (Center), and the t2 image $T_3 \circ \hat{h}_A$ (Right). Notice the remarkable correspondence between the transformed textbook and the desti-

nation patient A. Shown in the bottom row is the magnitude of the difference images between the transformed textbook and the substudies (top row minus the middle row).

Fig. 3 shows the result of estimating \hat{h}_B for patient B. The left column shows the MR spin-density (Upper) and t2 (Lower) images of patient B. The middle column shows the transformed textbook: $T_1 \circ \hat{h}_B$ and $T_3 \circ \hat{h}_B$. The right column shows the difference images demonstrating the near-perfect alignment.

Fig. 4 shows properties of the transformation \hat{h}_B . Fig. 4 Left shows the transformation applied to a rectangular grid, with Fig. 4 Center and Right showing the x and y components of the transformation. Bright areas in the displacement fields correspond to translation in the positive direction, and dark areas to translation in the negative direction. The mixture of low- and high-frequency components of the transformation are a result of the low- and high-dimensional transformation. Generating the transformation required 3 min of computation time on a 64×64 processor DECmpp 12000Sx/model 200 (MasPar).

Fig. 5 demonstrates the course to fine procedure, showing the global as well as local flow of information as the t2 component of the textbook aligns with patient A. Fig. 5 Left shows the magnitude difference between the textbook t2 component and patient A before any transformation. Notice the large disparity in global as well as local structure. Fig. 5 Center shows the correspondence after the application of the global transformation alone. Fig. 5 Right shows the difference after both the global and local transformations are applied. Notice that the local transformations allow for small adjustments of the fine substructures.

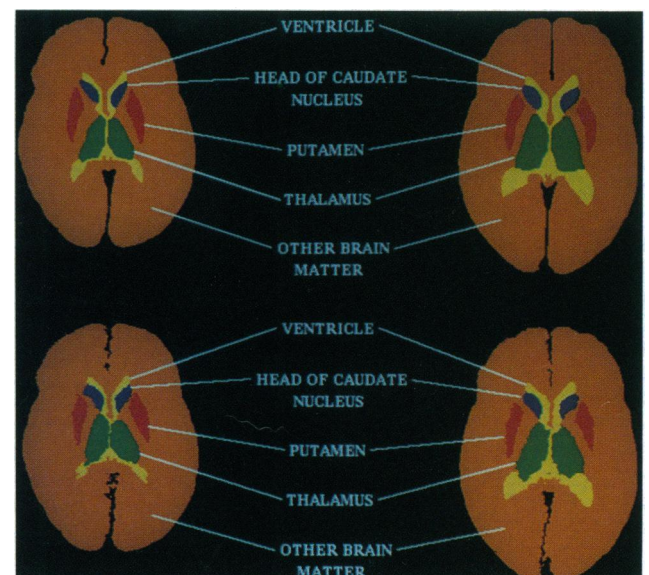


FIG. 6. (Upper) Hand-labeled structures of patients A (Left) and B (Right). (Lower) Automatically labeled structures of patients A (Left) and B (Right).



FIG. 7. (Left) True PET tracer distribution. (Center) Smoothed-maximum *a posteriori* PET reconstruction incorporating the anatomical MR information. (Right) Smoothed estimate generated without using the anatomical information.

Once the transformations, \hat{h}_A and \hat{h}_B , from the coordinate system of the textbook to the studies of patients A and B have been found, the symbolic label information can be automatically mapped to the patients' coordinate system. Shown in Fig. 6 is the result of applying the anatomically labeled gray-matter nuclei and ventricle information in the T_4 component of the textbook to the brains of patients A and B. The top row shows hand-labeled structures of patients A and B, and the bottom row the automated segmentation and labeling of both patients A ($T_4 \circ \hat{h}_A$; Left) and B ($T_4 \circ \hat{h}_B$; Right).

Fusing Modalities. All of the information in the textbook becomes available in the patient study, allowing for the high-resolution anatomical information of the textbook to be fused with the physiologic studies of brain activity (14, 15). Fig. 7 demonstrates the fusion of the anatomical textbook information into the emission tomographic physiologic studies. For this fusion study a new simulated textbook and simulated patient study was generated. The simulated textbook consisted of a segmented image, a spin-density, and a t2-weighted MR image corresponding to the hand segmentation of the textbook of Fig. 1. Standard tissue parameters were taken to represent cerebrospinal fluid, gray matter, and white matter, with the images generated by using the spin-echo sequence used in the Duke study.

Three images were generated from the segmentation of patient B, the first and second being spin-density and t2-weighted images. The third component of the patient study was a PET scan simulated to correspond to the Super-PET time-of-flight imager (16). Fig. 7 shows the result of incorporating the anatomic information of the deformed textbook—via the MR images—into the PET reconstruction. Shown in Fig. 7 Left is the true PET tracer distribution used for the study. Fig. 7 Center shows use of the anatomic information obtained via registration of the MR textbook with the patient for the calculation of the maximum *a posteriori* estimate of the PET tracer distribution. For this, a Good's roughness MRF prior (17) was used to locally smooth independently over the nuclei and ventricle areas. Notice the exquisite detail and tracer accuracy in the PET reconstruction. Fig. 7 Right shows the result of the same PET reconstruction algorithm with Good's smoothing globally applied across the boundaries of the anatomically distinct nuclei, without the use of the anatomic MR information. Notice how much anatomical detail, or resolution, is lost.

Conclusions

Projects such as the NLM's Visible Human project for the construction of digital anatomical libraries for two complete humans has to a large part motivated the work proposed herein. Thus far, only normal neuroanatomy has been discussed, although the methods must be extended to include the abnormal variation associated with disease. Again quoting from the NLM: "NLM should expand upon initial image

libraries comprised of normal structure to encompass specialized image collections which represent structural information, such as embryological development, normal and abnormal variations and disease-related images."

The construction of digital anatomical textbooks is quickly becoming a reality. Being able to transform the coordinate system of the textbook into that of any patient allows for sensor fusion as well as segmentation. All of the anatomic, histologic and pharmacologic information in the textbook then becomes available in the study of the individual.

We are indebted to Dr. Scott Nadel (Duke University) for the MR data, to Richard Rabbitt for help on the continuum mechanics, and to Marcus Raichle and Michael Vannier for helpful discussions during the development of the manuscript. M.I.M. and G.E.C. were supported by the National Institutes of Health (RR-1380), Office of Naval Research (N00014-92-J-1418) and Army Research Office (DAA 03-92-6-0141). Y.A. and U.G. were supported by the Army Research Office (DAAL-03-86-K-0110) and the Office of Naval Research (N00014-88-K-289).

1. Besag, J. (1974) *J. R. Stat. Soc. B* 36, 192–326.
2. Robb, R. A., ed. (1992) *Visualization in Biomedical Computing 1992* (SPIE, Bellingham, WA).
3. Terzopoulos, D. & Waters, K. (1990) *J. Visualization Comput. Animation* 1, 73–80.
4. Bajcsy, R. & Kovacic, S. (1989) *Comput. Vision Graphics Image Processing* 46, 1–21.
5. Amit, Y. (1993) *SIAM J. Sci. Comput.*, in press.
6. Grenander, U., Chow, Y. & Keenan, D. (1990) *HANDS: A Pattern Theoretic Study of Biological Shapes* (Springer, New York).
7. Amit, Y., Grenander, U. & Piccioni, M. (1991) *J. Am. Stat. Assoc.* 86 (414), 376–387.
8. Miller, M. I., Maffitt, D., Shrauner, J., Roysam, B. & Grenander, U. (1991) in *Proceedings of the Twenty-Fifth Annual Conference on Information Sciences and Systems*, eds. Davidson, F. & Goutsias, J. (Johns Hopkins Univ. Press, Baltimore), pp. 637–642.
9. Miller, M. I., Joshi, S., Maffitt, D. R., McNally, J. G. & Grenander, U. (1994) in *Statistics and Imaging*, ed. Kanti, M. (Carfax, Abingdon, Oxfordshire, England), Vol. 2, in press.
10. U.S. National Library of Medicine Board of Regents (1987) *National Library of Medicine, Long Range Plan: ELECTRONIC IMAGING* (DHHS, PHS, NIH, Bethesda, MD).
11. Segel, L. A. (1987) *Mathematics Applied to Continuum Mechanics* (Dover, New York).
12. Grenander, U. & Miller, M. I. (1994) *J. R. Stat. Soc. B* 56, in press.
13. DeArmond, S. J., Fusco, M. M. & Dewey, M. M. (1989) *Structure of the Human Brain: A Photographic Atlas* (Oxford Univ. Press, New York), 3rd Ed.
14. Pelizzari, C. A., Chen, G. T. Y., Spelbring, D. R., Weichselbaum, R. R. & Chen, C. T. (1989) *J. Comput. Assisted Tomogr.* 13 (1), 20–26.
15. Raichle, M. E. (1990) *Science* 249, 1041–1044.
16. Ter-Pogossian, M. M., Ficke, D. C., Yamamoto, M. & Hood, J. T. (1982) *IEEE Trans. Med. Imaging* 3, 179–187.
17. Miller, M. I. & Roysam, B. (1991) *Proc. Natl. Acad. Sci. USA* 88, 3223–3227.